IL NUOVO CIMENTO **41 C** (2018) 175
DOI 10.1393/ncc/i2018-18175-7

COLLOQUIA: IWM-EC 2018

Fission in inverse kinematics: A window to new experimental observables

M. CAAMAÑO(*)
IGFAE, University of Santiago de Compostela - E-15706 Santiago de Compostela, Spain

received 3 December 2018

Summary. — Experimentally, the understanding of the complex and intricate process of nuclear fission is approached by collecting as many observables as possible and from all fissioning systems available. The measured properties of the fissioning system and of the fission products, and their correlations, has led to the current picture where, in a very simplified way, the fission proceeds according certain modes or channels centred around fragments with particular numbers of protons and/or neutrons, which emerge with specific deformations that also drive the sharing of part of the available energy. Most of the information on fission was gathered so far in experiments that use direct kinematics, where the fissioning system can be considered at rest in the laboratory. However, these experiments suffer from two main drawbacks: few observables are measured simultaneously and the fragment atomic number is either absent or poor in resolution. The use of inverse kinematics, where the fissioning system is studied in-flight, opens a possibility to solve those issues and to add new information.

1. – A (very) brief history of fission

Almost eighty years ago, fission was first reported by Meitner and Frisch [1]. They described the process as the splitting of unstable uranium nuclei into two fragments of "*roughly equal size*" that repel each other with a kinetic energy of approximately 200 MeV. Within months, Bohr and Wheeler laid down the foundations of the accepted understanding of fission, including the formulation of fission barrier, the concept of "fissility", and also transitional levels and resonance neutron capture [2]. However, this early theoretical description, which treated the nucleus as charged liquid drop, lacks a key aspect of fission in actinides: instead of producing two fragments similar in size, the fragment distribution was experimentally found to be asymmetrical [3], with the fragments more likely to be of different size. In addition, systematic measurements showed

(*) E-mail: manuel.fresco@usc.es

that the heavy fragment has an average, fixed mass around $A \sim 139$, while the light fragment takes the rest of the total mass [4]. With the recent discovery and description of nuclear shells, it was tempting to see a link between these modes and the existence of preferred nucleon shells driving the formation of fragments [5].

The next natural step was to include nuclear structure into the description of fission. Strutinsky led the way by modifying the potential energy of the liquid-drop model with shell corrections and pairing terms [6]. The potential landscapes calculated in this way revealed a number of features: the fission barrier becomes a complex object with a height that depends on the mass partition of the fragments, higher for symmetric splits than asymmetric ones [7], while the potential at the scission points favours fragments with specific numbers of protons and neutrons with specific deformations [8].

Experimental data is consistent with this picture: a detailed analysis of the accumulated experimental data decomposes the fragment distribution in different modes and identifies two main asymmetric ones centred around $A \sim 132$ and $A \sim 140$ [9]. The total kinetic energy (TKE) distribution shows an increase around $A \sim 132$, which is understood as the result of a closer distance between fragments [10] due to the low deformation of one of them. The post-scission neutron evaporation has a minimum multiplicity around $A \sim 132$, consistent with a low deformation and intrinsic energy [11]. Together, these observations paint a picture where a heavy fragment, relatively cold and spherical, is formed preferably around the doubly closed-shell ^{132}Sn. However, while this interpretation could only be confirmed with the direct measurement of the proton and neutron contents of the fragments, fission data were vastly measured in terms of fragment masses.

1˙1. *Fission in inverse kinematics.* – The situation changed in the late 90s with the pioneering experiments done at GSI (Germany) by the group of K.-H. Schmidt and collaborators [12]. In these experiments, the fissioning nuclei are produced through fragmentation reactions and identified with the FRagment Separator (FRS) spectrometer. Fission was then induced in-flight through Coulomb interaction with a heavy target. The high-velocity boost allows the fragments to pass through different detectors where the energy loss and total energy can be measured. With this setup, the atomic numbers (Z) of the full fragment distribution could be identified for the first time. The results of this campaign revealed new features that did not fit within the then-standard picture of fission. The most prominent one was the fact that, when analysed in Z distributions, the asymmetric components of the heavy fragments are fixed at $Z \sim 52$ and $Z \sim 55$ [13], something unexpected considering that neutron shells were predicted as stronger than proton shells and that there was little indication of any influence of ^{132}Sn.

Coulomb-induced fission in inverse kinematics at GSI continues nowadays with the SOFIA experiment [14]. The new generation of experiments adds the ALADIN spectrometer at the end of the flight path of fragments in order to measure not only the atomic number but also the mass of both fragments in coincidence. The main difficulties of this approach are the high velocity of the fragments, which prevents a precise transformation of the centre of mass of the fissioning system, and the Coulomb interaction, which does not permit to measure the fission excitation energy.

Before SOFIA, the first experiment to measure the atomic number and the mass of the full fragment distribution was the VAMOS fission campaign at GANIL (France). In this case, the fissioning nuclei are produced by transfer and fusion reactions between a ^{238}U beam and a light target, typically carbon, at an energy just above the Coulomb barrier. The measurement of the light, target-like recoil allows to reconstruct the binary transfer

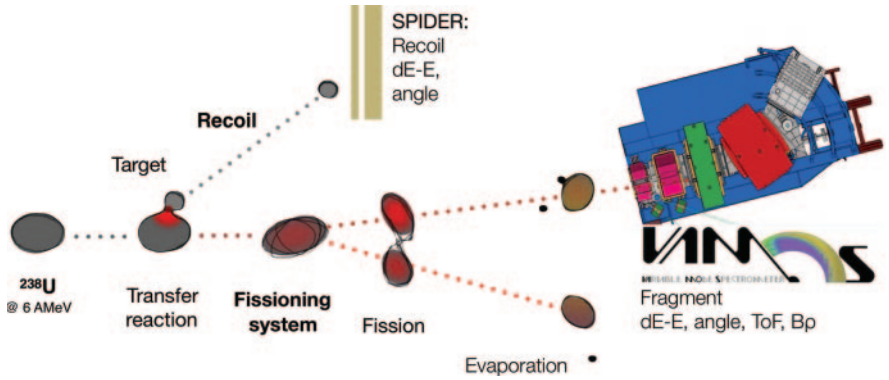

Fig. 1. – Schematic design of the experimental setup of the VAMOS fission campaign. A ^{238}U beam at 6 AMeV impinges on a light target and a transfer reaction occurs. The target light recoil is detected in the SPIDER detector, a set of double-sided stripped silicon detectors, where the energy and energy loss, as well as the recoil angle are measured. The fissioning system decays in-flight and one of the fragment enters the VAMOS spectrometer, where the time-of-flight, the magnetic rigidity, the energy and energy loss, and the emission angle are measured.

reaction and thus to assign a velocity vector and excitation energy to an isotopically identified fissioning system. The fission fragments enter the VAMOS spectrometer [15], where their velocity vector is measured along their Z, A, and charge state. Figure 1 shows a schematic representation of the experimental method. A more detailed description of the experimental setup can be found in [16,17]. In the following sections, we review some of the recent results of the VAMOS campaign at GANIL.

2. – New and revisited fission observables

One of the advantages of transfer- and fusion-induced fission is the possibility of studying different fissioning nuclei at different excitation energies. In the case of the VAMOS campaign, a set of nuclei between ^{238}U and ^{250}Cf were produced with average excitation energies between $E^* = 7$ and 46 MeV [17].

2˙1. *Isotopic and isotonic distributions.* – As we described in the previous section, inverse kinematics allows the fragments to go through a set of detectors thanks to the velocity boost acting upon the fissioning system, facilitating the measurement of the mass and atomic number of the fragments. In this way, the fragment yield distribution can be revisited in terms of the number of protons (Z) and in terms of the number of neutrons (N) of the fragments. The data from the VAMOS campaign permits to compare these distributions for different systems and different excitation energies, as is shown in fig. 2.

The Z distribution of fig. 2, left shows the expected constant position of the heavy fragment, already reported in [13], as a feature that remains even for high excitation energy. The underlying structure effects responsible for the preferred production of $Z \sim 52$ are supposed to vanish with increasing excitation energy. However, we can observe that, even in the case of fission of ^{250}Cf at $E^* = 46$ MeV, the yield distribution is not yet the Gaussian-like distribution that a structure-less, liquid drop behaviour would produce. Structure effects seem to survive at very high E^*.

The N distribution of fig. 2, right is more difficult to read because the measured

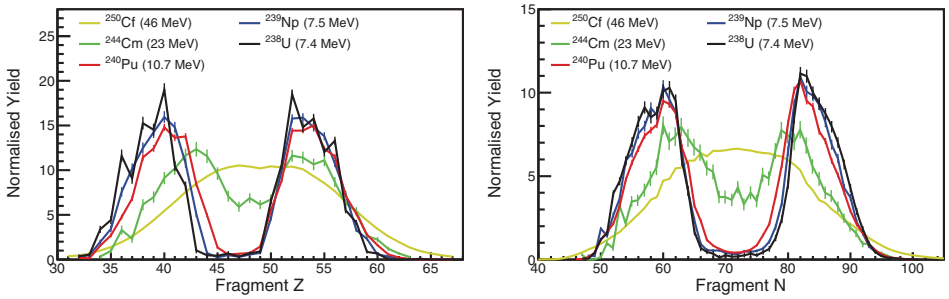

Fig. 2. – Normalized yield distributions of fragment Z (left) and N (right) from transfer- and fusion-induced fission. Data from [17].

neutron contents do not correspond to the ones produced at the scission point: between their production and their measurement, fragments release the excess of energy above their ground state in the form of neutron and gamma emission. However, we can observe that the light and heavy peaks of the distribution tend to approach with increasing E^*. Since neutron emission can only reduce the N of the fragments, this observation implies a larger neutron evaporation for the heavy fragment with increasing E^*, which is consistent with the recently proposed energy sorting mechanism, where the difference in level density forces the heavy fragment to accumulate the excess of E^*, increasing its neutron evaporation [18].

2˙2. *Neutron excess distributions*. – The fact that Z and N are measured in coincidence and event-by-event for all the detected fragments allows us to build a new observable: the neutron excess, or number of neutrons per proton, N/Z. Figure 3 shows the neutron excess for the set of systems produced in the last VAMOS campaign.

By construction, the N/Z is an observable sensitive to structure effects. We can observe in fig. 3 that low-energy fissioning systems display pronounced features that gradually disappear as E^* increases. The clearest feature is the large oscillation towards the $Z = 50$, $N = 82$ crossing point, which suggest a preferred combination of protons and neutrons around ^{132}Sn for the heavier fragment. The crossing of spherical shells $Z = 44$, $N = 64$ also appears as an accumulation point for the majority of the systems. As we

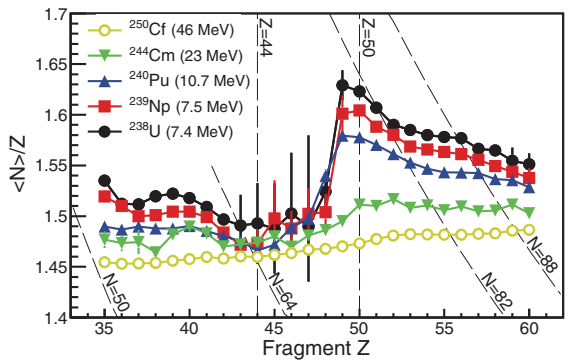

Fig. 3. – Neutron excess distribution of fragments produced in transfer- and fusion-induced fission. Dashed lines signal some relevant spherical and deformed shells. Data from [19].

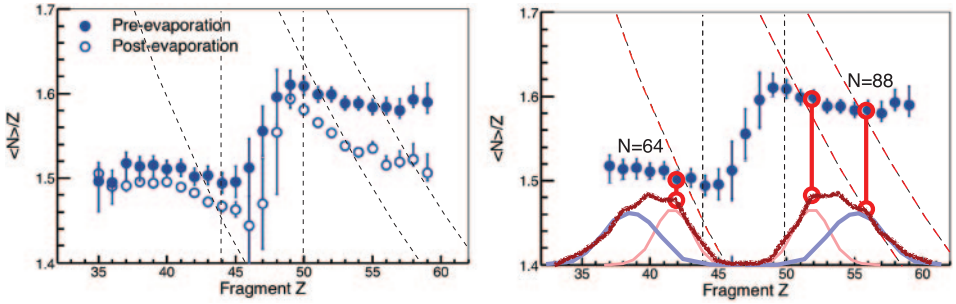

Fig. 4. – Left: Neutron excess of ^{240}Pu fission at $\langle E^* \rangle = 9$ MeV before (solid symbols) and after (empty symbols) post-scission neutron evaporation. Dashed lines correspond to the deformed and spherical shells depicted in fig. 3. Right: Neutron excess at scission (solid symbols) and fragment yield distribution in arbitrary units (overlayed solid dark-red line). The asymmetric fission yield modes are shown with light red and light blue lines. The circle-ended red lines connect the mean position of the fission modes with the measured N/Z at scission.

mentioned before, the preference for particular combinations disappear for increasing E^* as we can see in the case of ^{250}Cf, where the N/Z distribution is featureless and almost flat.

2˙3. *Back to the scission point.* – The N/Z distributions displayed in fig. 3 were obtained with the neutron and proton contents of the measured fragments and therefore they are also affected by neutron evaporation. In order to recover the actual mass of the fragments before neutron evaporation, we translate the velocity vectors of the fragments to the reference frame of the fissioning system and apply momentum conservation. This allows us to deduce not only the fragment mass at scission, but also other quantities, such as the total kinetic energy (TKE), the total excitation energy (TXE), and the neutron multiplicity (see [20] for further details).

Figure 4, left shows the comparison of N/Z before and after neutron evaporation for the case of ^{240}Pu at $\langle E^* \rangle = 9$ MeV. We can see that the main features of the N/Z distribution remain at scission, in particular the tendency to approach ^{132}Sn closed shells. However, we should recall that the fact that $N = 82$ is the preferred neutron content of fragments with $Z = 50$ does not imply that this particular combination is more produced than the others. This is clearly confirmed in fig. 4, right where the fragment yield is showed together with the N/Z distribution at scission. We observe that the asymmetric modes, fitted to the Z distribution, are centred around deformed $N = 64$ and $N = 88$, and spherical $N = 82$ shells. The measured N/Z at scission and the fragment yield distribution suggest then that the production is driven by neutron shells rather than proton shells. In addition, the influence of ^{132}Sn on the production is reduced since the $Z = 50$ does not seem to play any relevant role, only the $N = 82$ neutron shell. And even the role of this spherical shell acts on the same fission mode as the $N = 64$ shell on the light fragment, blurring the relative weight of each shell on the production of this mode. In order to determine which of these two shells is actually driving the production, we address the dynamics of the process in the following section.

Let us leave this section with two quick notes: firstly, this result seems to be in disagreement with the constant $Z = 52$, $Z = 55$ components found in the first inverse kinematics campaign at GSI [13] and the constant mass components found in classical experiments [4]. The ongoing analysis of a larger systematic measurements with systems

in a range of initial N/Z will help to clarify this apparent contradiction. Secondly, we should be careful when we compare relevant acting shells to the neutron or proton contents of the fragments. The neutrons or protons contained within the fragments build the shells before the scission point, and thus, once the break of the neck happens, the excess of neutrons and protons in the neck are shared between the fragments in a stochastic way, slightly modifying the formed shells. This is one of the reasons we assign shells to approximate proton and neutron numbers in the fragments.

3. – Fission dynamics and scission configuration

As we mentioned in the previous section, the use of momentum conservation on the reference frame of the fissioning system allows to calculate the total kinetic and excitation energy (TKE and TXE), as well as the neutron evaporation, as a function of the fragment Z. Since the TXE is released after scission in the form of neutron and gamma evaporation, the neutron multiplicity can be used to estimate the partition of TXE between the fragments under assumptions already proven experimentally. Figure 5, left shows the partition of TXE between the fragments produced in ^{240}Pu fission at $\langle E^* \rangle = 9\,\text{MeV}$ [21] compared with a recent, state-of-the-art calculation from a real-time microscopic model [22]. The access to the fragments E^* and its comparison with models is a very stringent test of the description of the underlying dynamics of the process. In this case, we can see that the calculations of [22] overestimate the influence of the ^{132}Sn and predict the region around $Z = 52$ populated by low E^*, cold, undeformed fragments.

The fragment E^* is the sum of intrinsic and deformation energy. The sources for the intrinsic energy are the initial E^* above the fission barrier and the dissipated energy between the saddle and scission points. The dissipation occurs when nucleon pairs are broken due to the levels crossing with evolving deformation. The ratio between odd- and even-Z fragments is a consequence and a measure of this dissipated energy [23]. In this case, we have used both the even-odd effect in the measured yields and a previous systematic on TXE to cross-check the deduced dissipation energy. The resulting intrinsic energy per fragment is displayed in fig. 6(b). Once the intrinsic energy can be determined,

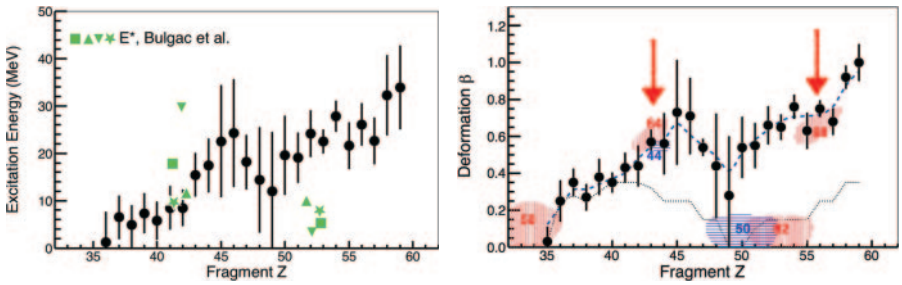

Fig. 5. – Left: Experimental mean excitation energy of fragments of ^{240}Pu fission at $\langle E^* \rangle = 9\,\text{MeV}$ (black symbols) compared with calculations of a model based on time-dependent energy density functional [22] (green symbols). Right: Deduced quadrupole fragment deformation. The hatched areas correspond to local minima of the potential energy at scission for proton (red vertical hatched lines) and neutron (blue horizontal hatched lines) levels [8]. The red arrows point to the mean position of the fission modes displayed in fig. 4. The dotted line corresponds to the mean deformation at the ground state of the fragments while the long-dashed line is a moving average of the measured points.

the remaining of fragment E^* corresponds to deformation energy.

In order to calculate the actual deformation from the corresponding energy, we need to know which is the main order that shapes the fragments. Traditionally, it has been assumed that quadrupole deformation is in average a good description of the fragments at scission [8,24]. However, recent theoretical models predict octupole or even more complex deformations as the main ones [25, 26]. In the following, and while the discussion is being settled, we can assume that the deformation energy is transformed into quadrupole elongation. Figure 5, right shows the deduced quadrupole deformation as a function of the fragment Z, for the ^{240}Pu data. We can observe that the distribution has also an oscillating behaviour that crosses the deformed shells $N = 64$, $N = 88$, and $Z = 44$, while wandering far from the spherical $Z = 50$ and $N = 82$. This is consistent with fig. 4, right where shells $N = 64$, $N = 82$, and $N = 88$ appeared correlated with the positions of asymmetric modes. Together, the N/Z at scission and the quadrupole deformation distributions suggest that the most relevant shells for the fragment production are $N = 64$ and $N = 88$ neutron deformed shells.

3˙1. *A picture of scission: shapes and energy.* – The measured TKE at scission corresponds to the Coulomb repulsion between the fragments at the scission point. From the deduced fragment shapes and a reasonable estimation of any pre-scission kinetic energy (see [21] for details), the distance between the fragments at scission can be calculated. In a first approximation, the tip distance —the distance between the surface of the fragments— corresponds to the length of the neck connecting the fragments right before scission. Figure 6(a) shows the tip distance between the fragments for the ^{240}Pu fission data. We can see a clear minimum around the $Z_1 = 52$, $Z_2 = 94 - 52 = 42$ split, which suggests a connection between a short neck and structure effects.

The tip distance and the quadrupole deformation are sufficient to describe the geometrical configuration of every split; together with the intrinsic excitation energy, they paint a complete picture of the scission point in terms of shapes and energy. The Right-hand side of fig. 6 displays the scaled configuration of a collection of fragment splits. The results range from very asymmetric splits between a cold, light fragment and a hot, very

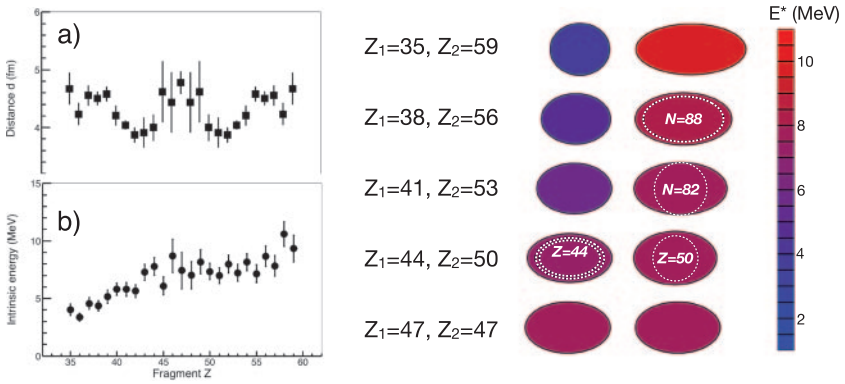

Fig. 6. – (a) Tip distance between the fragments. (b) Intrinsic energy. Right-hand side: Schematic representation of a set of five different fragment splits. The shape and distance between the ellipsoids are scaled values of the calculated ones from the experimental data. The colour code represents the intrinsic excitation energy stored by the fragments. Relevant spherical and deformed shells are also inscribed within the corresponding fragments.

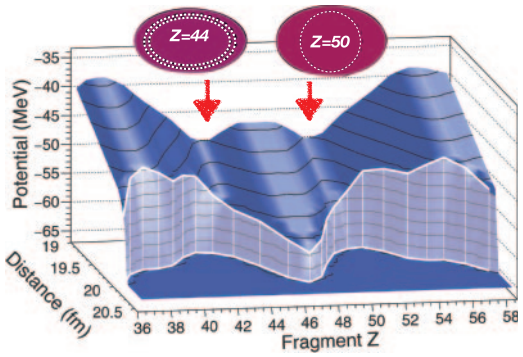

Fig. 7. – The sum of the TXE and the deformation energy at scission, marked as Potential, is plotted as a function of the distance between fragment centres and the fragment Z. The actual data corresponds to the white line following the edge of the surface. The Potential surface behind the white line is a linear extrapolation to guide the eye. The fragment shapes and shells for the $Z_1 = 44$, $Z_2 = 94 - 44 = 50$ split are shown for reference.

deformed heavy partner to a in-between excited and deformed symmetric split.

A final picture can be constructed from the distance between the fragments and the TXE. The potential energy landscape is usually discussed in terms of elongation, fragment asymmetry, and potential energy. Throughout this work, we have shown the experimental measurement of the fragment asymmetry and the TXE, and the derivation of the deformation energy and the distance between the fragments. Considering the potential energy as the sum of the TXE and the deformation energy, we can build the shape of the potential landscape at scission as shown in fig. 7.

The edge of the surface depicted, which corresponds to the scission line, is consistent with a path of minimum potential around the $Z_1 = 44$, $Z_2 = 94 - 44 = 50$ split, which can be interpreted as a fission mode "carved" by the effect of neutron $N = 64$ and proton $Z = 44$ deformed shells. Incidentally, and according to the results discussed in the previous sections, the presence of $Z = 50$ seems merely accidental. The fact that the most important shells seem to be deformed is consistent with the survival of these effects up to high initial excitation energy, as we discussed in previous sections and in fig. 1.

4. – Summary and perspectives

After almost eighty years, the experimental study of the fission process is nowadays being boosted by the use of inverse kinematics. This technique allows the complete identification of the full fragment distribution, which, in coincidence with the measurement of the fragment velocity, opens a window to revisit classical observables and build new ones.

The study of isotopic fragment yields reveals that structure effects survive up to very high initial excitation energy. In addition, the measurement of the neutron excess shows a preference to approach the double closed shells of ^{132}Sn. However, while this is a preferred combination of neutrons and protons, it is not the most produced. The combined study of neutron excess at scission and isotopic fragment yields suggests that neutron shells are the ones driving the fission process.

The accurate measurement of the initial excitation energy that transfer reactions provide allows the fission campaign at VAMOS/GANIL (France) to measure the total

kinetic and excitation energy at scission, and to deduce the intrinsic and deformation energy. The quadrupole fragment deformation singles out again the role of deformed neutron shells in the fission yields, which is also consistent with their survival at high initial excitation energy.

Finally, these considerations were based on the results from ^{240}Pu fission alone. It is expected that a systematic study with the complete set of measured fissioning systems will sharpen these conclusions and add additional information, such as the evolution of the influence of structure on the process with the excitation energy and the fissioning system.

* * *

The author acknowledges the financial support of the Program Ramón y Cajal of the Ministerio de Economía y Competitividad of Spain through the grant number RYC-2012-11585. The author is also deeply grateful to F. Farget and D. Ramos, as well as to the VAMOS team at GANIL, for the continuous support.

REFERENCES

[1] Meitner L. and Frisch O. R., *Nature*, **11** (1939) 239.
[2] Bohr N. and Wheeler J. A., *Phys. Rev.*, **56** (1939) 426.
[3] Booth E. T. *et al.*, *Phys. Rev. C*, **55** (1939) 982.
[4] Flynn K. F. *et al.*, *Phys. Rev. C*, **5** (1972) 1725.
[5] Mayer M. G., *Phys. Rev.*, **74** (1948) 235.
[6] Strutinsky V. M., *Nucl. Phys. A*, **95** (1967) 420.
[7] Pashkevich V. V. *et al.*, *Nucl. Phys. A*, **169** (1971) 275.
[8] Wilkins B. D. *et al.*, *Phys. Rev. C*, **14** (1976) 1832.
[9] Brosa U. *et al.*, *Phys. Rep.*, **197** (1990) 167.
[10] Britt H. C. *et al.*, *Nucl. Instrum. Methods A*, **24** (1963) 13.
[11] Wahl A. C., *At. Data Nucl. Data Tables*, **39** (1988) 1.
[12] Schmidt K.-H. *et al.*, *Nucl. Phys. A*, **665** (2000) 221.
[13] Böckstiegel C. *et al.*, *Nucl. Phys. A*, **802** (2008) 12.
[14] Pellereau E. *et al.*, *Phys. Rev. C*, **95** (2017) 054603.
[15] Pullanhiotan S. *et al.*, *Nucl. Instrum. Methods A*, **593** (2008) 343.
[16] Caamaño M. *et al.*, *Phys. Rev. C*, **88** (2013) 024605.
[17] Ramos D. *et al.*, *Phys. Rev. C*, **97** (2018) 054612.
[18] Schmidt K.-H. and Jurado B., *Phys. Rev. Lett.*, **104** (2010) 212501.
[19] Ramos D. *et al.*, *EPJ Web of Conferences*, **111** (2016) 10001.
[20] Caamaño M. *et al.*, *Phys. Rev. C*, **92** (2015) 034606.
[21] Caamaño M. and Farget F., *Phys. Lett. B*, **770** (2017) 72.
[22] Bulgac A. *et al.*, *Phys. Rev. Lett.*, **116** (2016) 122504.
[23] Rejmund F. *et al.*, *Nucl. Phys. A*, **678** (2000) 215.
[24] Goddard P. *et al.*, *Phys. Rev. C*, **92** (2015) 054610.
[25] Sadhukhan J. *et al.*, *Phys. Rev. C*, **96** (2017) 061301(R).
[26] Scamps G. and Simenel C., arXiv:1804.03337 [nucl-th] (2018).